Quantifying fatigue overload retardation mechanisms by energy dispersive X-ray diffraction

Simpson, C.A[a,b,e,*], Kozuki, S[c], Lopez-Crespo, P[a,d], Mostafavi, M[e], Connolley, T[f], Withers, P.J[a,b]

[a]*School of Materials, University of Manchester, Manchester, M13 9PL, UK*
[b]*Manchester X-Ray Imaging Facility, Research Complex at Harwell, RAL, Didcot, OX11 0FA, UK*
[c]*JFE Steel Corporation, Japan*
[d]*Department of Civil and Materials Engineering, University of Malaga, C/Dr Ortiz Ramos s/n, 29071 Malaga, Spain*
[e]*Department of Mechanical Engineering, University of Bristol, Queen's Building, University Walk, Bristol, BS8 1TR UK*
[f]*Joint Engineering, Environment, and Processing Beamline, Diamond Light Source, Didcot, OX11 0DE, UK*

Abstract

The fatigue crack retardation mechanisms operating after an overload event are investigated for a bainitic steel using high spatial resolution energy dispersive synchrotron X-ray diffraction. The elastic crack-tip strain fields are mapped at mid-thickness of compact tension samples at R-ratios of 0.1 and 0.4. The same overload stress intensity factor ($K^{OL} = 60\,\mathrm{MPa\,m^{1/2}}$) is applied in each case with the cracks then propagating under the same applied stress intensity range, $\Delta K^{app} = 27\,\mathrm{MPa\,m^{1/2}}$. The competing retardation mechanisms are directly quantified and separated, with the associated fatigue crack growth (FCG) rates then being predicted according to a 2-parameter Walker-type assessment and validated against those measured. The stress intensity factor associated with the overload residual stress field is calculated using a weight function approach. For $R = 0.1$, shielding from residual stress controls retardation when crack growth through the overload plastic zone, r_p^{OL}, is small (specifically $< 0.6\,r_p^{OL}$). For more extensive crack growth, discontinuous crack closure controls the retardation behaviour, with significant load transfer across opposing crack faces being observed at minimum load (for $R = 0.1$). These crack face tractions are associated with the plastic asperity created during overload. The traction forces holding the crack faces open at minimum load are, for the first time, used to directly quantify the associated stress intensity factor, K_{min}^{tract} as a function of crack growth. While no crack shielding is expected, nor observed, for $R = 0.4$, the variation in FCG rate after overload is explained by changes in effective R-ratio.

Keywords: crack opening displacement, linear elastic fracture mechanics (LEFM), crack-tip shielding, intrinsic shielding

1. Introduction

Subcritical fatigue crack growth (FCG) is conventionally understood according to linear elastic fracture mechanics (LEFM), which provides us with parameters such as the stress intensity factor, K, that characterise the conditions experienced at the crack-tip. These parameters are defined by direct, accessible macroscale measurements of variables such as the applied load, P^{app}, sample geometry and crack length. This serves as a convenient and, broadly speaking, reliable method by which to understand and ultimately predict FCG. However, problems arise in non-trivial cases where the intrinsic, material dependent FCG response can no longer be considered in isolation but must be assessed with respect to extrinsic factors. Examples of these extrinsic factors, or shielding mechanisms, include plasticity induced closure [1], discontinuous closure [2], crack bridging [3] and residual stresses [4, 5]. While LEFM may still be fundamentally applicable in these non-trivial cases, it is no longer sufficient simply to consider the applied stress intensity factor range, which is to say ΔK^{app} no longer adequately characterises the crack-tip conditions. In such cases it is insightful to identify

*Corresponding author: c.simpson@bristol.ac.uk

the effective stress intensity factor range, ΔK^{eff}.

In order to correctly characterise ΔK^{eff} it is useful to consider the impact of different types of shielding mechanism. While there are a great number of potential mechanisms (as categorised and detailed by authors such as Ritchie [6]), the likely contribution from each of these is determined by the material system, environment and stress intensity range under which the crack is propagating [17]. In simple metallic systems, residual stresses, PIC and discontinuous closure are the most commonly observed overload retardation mechanisms and have been subject to most scrutiny [5, 8, 18, 19]. The anticipated impact of overload residual stresses and discontinuous closure on K^{eff} can be seen in Fig. 1.

Plasticity induced closure (PIC), as first defined by Elber [1], is thought to play a significant role in FCG (and overload FCG [8]). In-elastic dilations of material in the plastic zone lead to local, premature crack face contact in the immediate vicinity of the crack-tip [1, 7, 9]. This behaviour is often used to explain the impact of R-ratio on FCG rates and has been described analytically by authors such as Budiansky and Hutchinson [10] and Newman [11]. While this phenomenon is well characterised and accepted for material in a plane stress state, it has remained contentious for material under plane strain conditions due to an absence of available material required for the self consistent volume flow. Authors such as Pippan contest that under plane strain conditions you have shear and volume rotation which allows for this contact [12].

As noted, PIC is a continuous process acting local to the crack-tip. Fleck expanded this concept to encapsulate a related, discontinuous mechanism [2], whereby the crack is being wedged open by plasticity induced deformation or asperities that are no longer connected to the advancing crack front. This discontinuous closure is an important consideration in overload experiments, where significant, additional deformation is introduced during overload and left in the wake of the advancing crack front. This deformed wedge of material prevents crack-tip closure, limiting the effective stress intensity range. As Anderson asserts, this type of mechanism is more appropriately described as residual crack opening [7]. Discontinuous closure will only be observed when $K^{app}_{min} < K^{op}$, where K^{op} is a non-zero stress intensity factor that must be applied to achieve crack opening (see Fig. 1d). In such a case, the effective stress intensity factor range, ΔK^{eff} and effective R-ratio, R^{eff} are typically defined:

$$\Delta K^{eff} = K^{app}_{max} - K^{op} \tag{1a}$$

$$R^{eff} = \frac{K^{op}}{K^{app}_{max}} \tag{1b}$$

In addition to PIC and discontinuous closure, residual stresses have been shown to play a significant role determining the transient FCG behaviour after an overload event [5, 8]. The additional crack-tip plasticity and associated compressive residual stress field act to reduce the magnitude of the full stress profile, reducing both K_{min} and K_{max} (see Fig. 1b and Fig. 1c). While this does affect R^{eff}, it does not technically reduce ΔK. However, it is considered reasonable to discount the FCG contribution from the portion of the fatigue cycle that falls below $0\,\mathrm{MPa\,m^{1/2}}$ [4]. More specifically, if $K^{res} + K^{app}_{min} < 0$ then the crack driving force can be defined as follows:

$$\Delta K^{eff} = \Delta K^{app} - (K^{app}_{min} + K^{res}) \tag{2a}$$

$$R^{eff} = \frac{K^{app}_{min} + K^{res}}{K^{app}_{max} + K^{res}} \tag{2b}$$

This approach and understanding assumes that residual stresses only act in a region local to the process zone. Berghini et al. [13] rightly assert that residual stress fields may also work to promote closure in the far-field. In this work contact and closure are considered separate to residual stress effects.

As Fig. 1 illustrates, while residual stresses do not always reduce ΔK^{eff}, they will always affect R^{eff}. In material systems that display a significant dependence on R-ratio, a simple Paris type relationship between stress intensity factor range and FCG rate is not sufficient. A two-parameter description, where $da/dN = f(\Delta K, R)$, must instead be used. Walker was the first to propose such a relationship [14], although this and many of the early two-parameter formulations only accurately describe FCG behaviour at high R-ratios. More recently, work by authors such as Dinda and Kujawski [15] and Noroozi et al. [16] have extended this approach to both lower and negative R-ratios, typically by discounting any portion of the stress intensity profile that falls below zero.

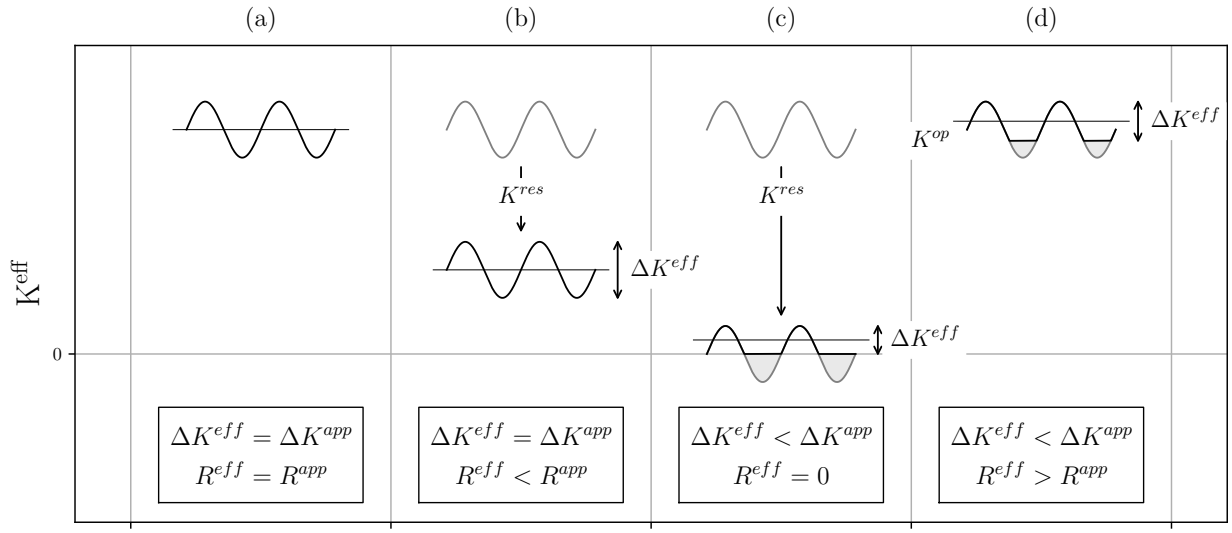

Figure 1: The impact of different shielding mechanisms on K^{eff}, ΔK^{eff} and R^{eff}. (a) The nominal, applied cyclic stress intensity factor profile, (b, c) the same applied stress intensity factor profile for a crack embedded in a compressive residual stress field and (d) a crack held open by discontinuous closure. In (b) $K^{res} + K^{app}_{min} > 0$ and in (c) $K^{res} + K^{app}_{min} < 0$.

To quantify the impact of overload and to reach a point where we can properly define and potentially predict ΔK^{eff}, we need to be able to accurately measure the crack-tip stress field and any far-field effects (such as that from closure). Internal residual stress fields can be directly interrogated through techniques such as neutron diffraction and X-ray diffraction (XRD), but the former has been limited by poor spatial resolution [20] and the latter [21] by poor depth penetration such that only the surface state could be interrogated. However, the advent of high energy, third generation synchrotron X-ray sources has made XRD a viable measurement technique even on thicker, plane strain, steel samples [19]. XRD experiments benefit from a high spatial resolution due to the comparatively fine aperture size that can be used ($\leq$50 µm). This has allowed for a number of ground breaking crack-tip strain measurement experiments to be conducted [18, 19, 22, 23]. One such experiment was carried out on a fine-grained bainitic steel by Lopez-Crespo et al. [19]. They used the high energy, hard X-ray source found at the ID15 beamline at the European Synchrotron Radiation Facility (ESRF) to interrogate overload behaviour in thick compact tension (CT) samples; this was the first time that crack-tip stresses had been probed under plane strain conditions. Significantly, this work highlighted two phenomena which depended on the crack position relative to overload. The first of these was a reduction in peak opening elastic strain immediately after overload. This mean strain effect was consistent with a reduction in K^{eff} due to K^{res}, with no reduction in the total associated strain excursion. When the crack-tip had propagated beyond the overload location there was evidence of discontinuous closure and a reduction in effective strain range.

More recently Salvati et al. [8] attempted to separate the contribution from residual stress and plasticity induced closure by looking at FCG behaviour and stress fields after overload at $R = 0.1$ and $R = 0.7$. They used energy dispersive X-ray diffraction (EDXRD) to monitor the crack-tip strain profiles and validate their residual strain modelling work. The authors converted the reduction in growth rate to an equivalent retardation factor and considered the difference between the retardation curves to be the retardation due to plasticity induced closure.

Despite decades of study, fatigue crack growth behaviour after an overload is still poorly characterised. Quantification and separation of the active mechanisms is sorely needed and is a necessary step towards the accurate modelling and lifing of components subject to complex, variable loading. In this paper we aim to quantify, separate and better clarify the different, competing factors contributing to fatigue crack growth retardation after an over-

load. To that end we use EDXRD to measure and quantify the crack-tip strain fields and use them to evaluate the effect of closure and residual stress on fatigue crack growth at high and low R-ratios. Discontinuous closure is considered separate from PIC and is distinguished by crack face contact stresses that are discrete and distinct from the crack front. Closure and residual stress measurements are assessed in terms of their associated impact on K^{eff} and R^{eff} and are validated against measured fatigue crack growth rates.

2. Experimental Details

2.1. Material and samples

A fine-grained bainitic steel was provided by the JFE Steel Corporation; the composition of the steel is summarised in Table 1. A micrograph of the associated microstructure is shown in Fig. 2, with a grain size of approximately 10 µm being recorded. A tensile test according to ASTM E8 [24], with the sample cut from a plate orientated parallel to the crack opening orientation, demonstrated a yield stress of 570 MPa and an ultimate tensile stress of 680 MPa. CT specimens were extracted perpendicular to the same plate material with a thickness of 10 mm and a width of 62.5 mm, with other dimensions adhering to that prescribed by ASTM E647 [25]. The sample geometry is presented in Fig. 3b.

	C	Si	Mn	P	S
610E	0.5	0.19	1.42	0.12	0.005

Table 1: Nominal composition (weight %) of the bainitic steel provided by JFE (balance Fe).

2.2. Fatigue test

Prior to the in-situ FCG experiment, pre-cracks were introduced into the CT samples using a load shedding methodology at $R = 0.1$ according to ASTM E647 [25]. The final stress intensity factor range used in this initial pre-cracking was $11\,\mathrm{MPa\,m^{1/2}}$. The crack was then propagated, in-situ on the I12 (JEEP) beamline at the Diamond Light Source (DLS), for 0.5 mm to a crack length, $a_0 = 23.5\,\mathrm{mm}$ at $\Delta K^{app} = 27\,\mathrm{MPa\,m^{1/2}}$ and at an R-ratio defined by the subsequent FCG testing conditions (i.e. $R = 0.1$ and $R = 0.4$). The I12 beamline can accommodate a sophisticated 100 kN

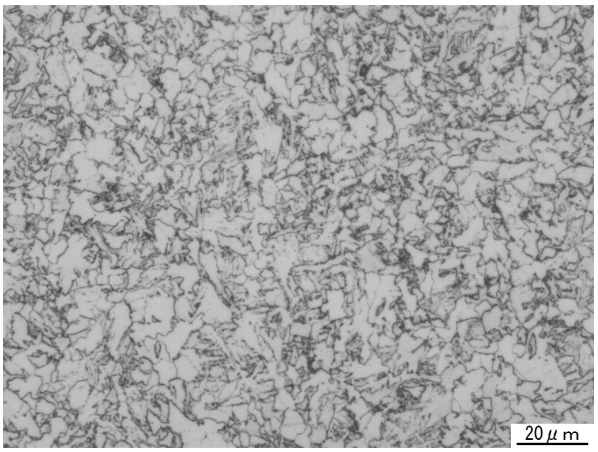

Figure 2: An optical micrograph of the bainitic steel showing a grain size of approximately 10 µm.

Instron servo-hydraulic rig. This rig is closely integrated into the beamline, which makes combined FCG testing and EDXRD acquisition straightforward. The overload and subsequent FCG experiment were completed in-situ on this test-rig at a loading frequency of 14 Hz.

Two FCG overload experiments were completed during the experimental run, one at $R = 0.1$ and one at $R = 0.4$. Previously, Borrego et al. [26] utilised $R = 0.05$ and $R = 0.25$ for their systematic study but did not observe a stark difference in FCG response. Testing at $R = 0.4$ was, however, expected to be governed by different controlling mechanisms than at $R = 0.1$ due to the crack faces being held further open at K^{app}_{min}. Both tests employed the same stress intensity factor range, $\Delta K^{app} = 27\,\mathrm{MPa\,m^{1/2}}$. K^{app}_{max} was $30\,\mathrm{MPa\,m^{1/2}}$ at $R = 0.1$ and $45\,\mathrm{MPa\,m^{1/2}}$ at $R = 0.4$ resulting in 0.29 mm and 0.66 mm forward plastic zones respectively (see Eqn. 3) which are negligible compared to the 39 mm uncracked ligament, ensuring the validity of an LEFM approach. A schematic of the fatigue cycling conditions can be seen in Fig. 3a.

The experiment was completed under constant or pseudo-constant ΔK^{app}, which is to say a load shedding technique was employed to maintain ΔK^{app} close to the required level of $27\,\mathrm{MPa\,m^{1/2}}$. The crack growth rate was monitored using an alternating current potential drop (AC-PD) system. The CT samples were subject to an overload to $K^{OL} = 60\,\mathrm{MPa\,m^{1/2}}$ at a crack length, $a_0 = 23.5\,\mathrm{mm}$. The overload stress intensity factor corresponded to overload factors of 2 and 1.33 at $R = 0.1$ and $R = 0.4$ respectively. The FCG

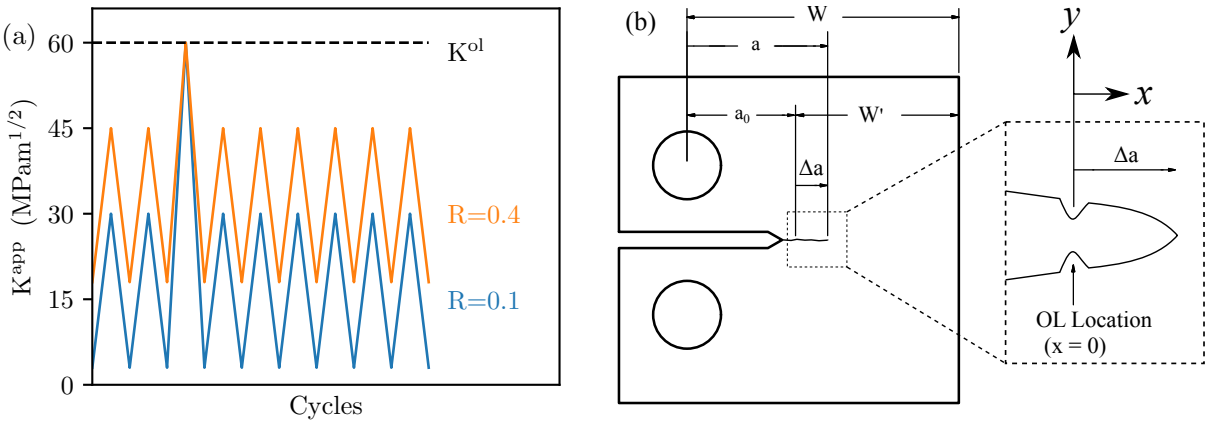

Figure 3: (a) Fatigue crack growth schematic for testing at $R = 0.1$ and $R = 0.4$ and (b) the associated geometry of the CT test samples. Note that (b) also features a magnified visualisation of the overload location, with the change in crack length (Δa) relative to the overload position ($x = 0$) being highlighted.

cycling at $R = 0.1$ fully satisfied the plane strain stress state criterion whereas at $R = 0.4$ it was not satisfied. However, using the EDXRD set-up we were able to illuminate and assess a gauge volume with a length in the z direction of 3.5 mm (for the fine measurements) [27]. This was centred at mid-thickness ($z = 0$) within the test specimen and, as such, the gauge volume can reasonably be assumed to sample material in a plane strain stress state.

When deciding upon the crack growth increments and associated positioning for the strain field mapping, it is important to consider the plastic zone sizes. The monotonic overload plastic zone should delimit the residual stress affected region and it is sensible to normalise crack growth increments with respect to this value. According to Irwin [28], the forward, monotonic plastic zone, r_p and reversed, cyclic plastic zone, r_c, in a plane strain stress state can be estimated according to the following relationships:

$$r_p = \frac{1}{3\pi}\left(\frac{K}{\sigma_{yield}}\right)^2 \tag{3}$$

$$r_c = \frac{1}{3\pi}\left(\frac{\Delta K}{2\sigma_{yield}}\right)^2 \tag{4}$$

The theoretical forward plastic zone size, r_p^{OL} at $K^{OL} = 60\,\mathrm{MPa\,m^{1/2}}$ is 1.17 mm. The analysis carried out in Section 4.1 suggests that the actual plastic zone size is slightly larger than this and the measured value of $r_p^{OL} = 1.4$ mm is used for the crack length normalisation.

The fatigue crack was grown in steps through, and ultimately beyond, the plastic zone generated by the overload, with strain maps being taken both immediately before and after overload and at four subsequent positions. These are summarised in Table 2. At each acquisition position the fatigue cycling was interrupted and the load held at the desired level; in each case maps at K_{min} were acquired after those at K_{max}. The strain mapping procedure is described Section 2.3.

After the in-situ FCG testing, the samples were removed and cooled in liquid nitrogen before being fractured. The fracture surfaces were assessed in a FEI Magellan 400 scanning electron microscope (SEM), with the pre-crack, overload (OL) and final crack lengths being measured for the AC-PD calibration. Fractographs were also taken across the sample thickness, with higher resolution imaging being carried out in and around the OL location.

2.3. X-ray diffraction and strain analysis

The elastic crack-tip strain at mid-thickness was mapped at the Diamond Light Source on the I12 (JEEP) beamline. A polychromatic (50 keV to 150 keV) beam was used and the diffracted beam captured using an array of 23 independent energy-dispersive detectors evenly spaced around the top half of the Deby-Scherrer cone [29]. The relative energy resolution of the detector elements ranges from 8×10^{-3} at 50 keV to 1.0×10^{-2} at

150 keV. The scattering take off angle, 2θ, was set at 5° and defined using two sets of collimating slits, with an associated angular resolution, $\Delta\theta/\theta = 3.2 \times 10^{-3}$. This set-up allowed for the acquisition of diffraction rings up to the {330} reflection. In an energy-dispersive arrangement the gauge volume over which strain is measured is fixed in space by the incoming and outgoing slits. To ensure the illuminated gauge volume was correctly located at the sample's mid-thickness, the sample was first translated through the illuminated volume. The points at which the diffracted signal first rise and then trail off are associated with the edges of the sample; once these are located the sample can be positioned at the mid-point between them.

The surface displacements and therefore the surface strains were measured simultaneously via digital image correlation (DIC). The experimental set-up and results are the subject of separate journal article [30], with surface (plane stress) overload retardation behaviour being compared against the internal (plane strain) response.

After each FCG stage a coarse and a fine 2D map were acquired at maximum and minimum load. The beam size was 50 µm square for the near crack-tip region and 100 µm square for the far-field region. The point spacing was 350 µm for the coarse map and 100 µm for the fine map. Additional line profiles were taken at intermediate loads during unloading from K_{max}; these line scans (in the x-direction, close to $y = 0$) utilised the fine aperture size and a point spacing of 150 µm.

To calculate the elastic strain, the acquired diffraction data must be compared against a stress-free equivalent. There are a number of accepted techniques for the acquisition of the stress-free lattice spacing, d_0 (see Withers et al. [31]) but in this case a far-field, stress-free position was chosen on the test sample. The elastic strain can then be determined in accordance with Braggs' Law, where

$$\epsilon_(\phi, hkl) = \frac{\Delta d_{(\phi,hkl)}}{d_{0(\phi,hkl)}}. \tag{5}$$

$\epsilon_(\phi, hkl)$ is the average lattice strain for the illuminated grains orientated such that their lattice plane of index hkl satisfies Braggs' law at an azimuthal angle, ϕ. The strain was calculated using an angle (detector) specific stress-free lattice parameter, $d_0(\phi, hkl)$, which has been shown to reduce the sensitivity to detector alignment and positioning [32]. The strain calculated from the eleventh detector in the array ($\phi = 90°$) is associated with the strain in the crack opening orientation, ϵ_{yy} and the first and final detectors ($\phi = 0°$ and $\phi = 180°$) are associated with the strain parallel to the crack ϵ_{xx}. The analysis was performed using the pyXe strain analysis package (v0.8.1) developed by Simpson [33], with the {110} peak being tracked and fitted to a Gaussian profile. The approach is described in more detail by Mostafavi et al. [34].

To calculate stress from the EDXRD diffraction data, one needs to know three orthogonal normal strain components [35]; in this case ϵ_{xx}, ϵ_{yy}, ϵ_{zz}. The associated co-ordinate system is highlighted on the fractographs in Fig. 5 and Fig. 6. While it is not possible to measure the strain along the beam direction (ϵ_{zz}), this can be inferred from the fact that the sample is thick and we are measuring a 3.5 mm mid-thickness slice and are therefore in a state of plane strain. Given this assumption, we can say that $\epsilon_{zz} = 0$. As such, the stress in the crack opening orientation as a function of position, $\sigma_{yy}(x, y)$, can be calculated using Eqn. 6:

$$\sigma_{yy}(x, y) = \frac{E'}{1 - (v')^2}(e_{yy} + v' e_{xx}) \tag{6}$$

where $E' = E_{hkl}/(1-v_{hkl}^2)$ and $v' = v_{hkl}/(1-v_{hkl})$. E_{hkl} and v_{hkl} are the diffraction elastic constants associated with the lattice plane being assessed. In this case the {110} reflection was tracked, with the associated diffraction elastic constants, $E_{110} = 226$ GPa and $v_{110} = 0.28$ being utilised (as per the Kroner modelling scheme) [35].

3. Results

3.1. Fatigue Crack Growth Results

FCG rates after overload and the associated mechanistic behaviour are assessed as a function of the (internal) crack growth, Δa beyond the overload location, a_0. This is considered to be a useful measure of the crack position, particularly when normalised against the overload plastic zone size, r_p^{OL}. This is a convenient, and generalised, approach to defining the extent and impact of overload retardation mechanisms (e.g. $\Delta a/r_p^{OL} = 1$ should indicate when the crack has grown through the residual stress field introduced by the overload).

The baseline fatigue crack growth behaviours (no overload) at $R = 0.1$ and $R = 0.4$ are presented in Fig. 4a. The crack growth rates show a small, but significant dependence on R-ratio.

When $\Delta K^{app} = 27\,\mathrm{MPa\,m^{1/2}}$ a growth rate of 9.5×10^{-5} mm/cycle was recorded at $R = 0.1$, and a rate of 1.3×10^{-4} mm/cycle was measured at $R = 0.4$. This baseline behaviour can be compared against the AC-PD measured growth rate recorded after overload, which is displayed in Fig. 4b. Note that the crack growth measurements recorded in Table 2 are slightly different from the values displayed in Fig. 4b. This is because the crack growth beyond overload measured by AC-PD, Δa_{av}, is an average through-thickness measurement, while the EDXRD values (Δa) are inferred from the synchrotron strain measurements which are weighted towards the mid-thickness and so are more representative. At $R = 0.4$ the crack front is straight and so in this case $\Delta a_{av} = \Delta a$.

While ΔK^{app} was nominally constant, the load shedding methodology employed during FCG allowed ΔK^{app} to vary between $25\,\mathrm{MPa\,m^{1/2}}$ and $28\,\mathrm{MPa\,m^{1/2}}$ during a typical growth increment. A small correction was therefore applied to the crack growth rates shown in Fig. 4b, accounting for the difference between the nominal and applied value of ΔK^{app} (ΔK^{corr}), while also considering the raw FCG growth rates, da/dN_{raw}, and an associated, approximate value of the effective stress intensity range, $\Delta K^{eff,approx}$:

$$\Delta K^{eff,approx} = \left(C^{-1} \frac{da}{dN}_{raw} \right)^{\frac{1}{m}}, \qquad (7)$$

$$\frac{da}{dN} = C \left(\Delta K^{eff,approx} - \Delta K^{corr} \right)^{m}. \qquad (8)$$

The Paris coefficients, C and m, were taken from the baseline fatigue crack growth rate data, which is shown in Fig. 4a. It should be stressed that this correction does not change the underlying trends observed in the data nor the magnitude of the recorded FCG rates, but does eliminate unrealistic variation in da/dN within each growth increment.

After overload the crack growth rate at $R = 0.1$ immediately dropped; there was no indication of an initial increase in growth rate prior to this retardation as has been noted by authors such as Borrego et al. [26]. This could be due to the comparatively low AC-PD acquisition rate, with the first data point being recorded after 200 cycles. After the initial retardation the growth rate slowly increased prior to a secondary, accidental overload ($K^{OLb} \approx 38\,\mathrm{MPa\,m^{1/2}}$) at $\Delta a_{av} = 0.85\,\mathrm{mm}$ (and $\Delta a/r_p^{OL} = 0.8$). This second overload caused a slight retardation in growth rate before it recovered and plateaued at approximately 2×10^{-5} mm /cycle. The growth rate did not recover to the initial baseline value and does not appear to be tending towards it. An estimate of the growth behaviour without the secondary overload is also depicted in Fig. 4b. At $R = 0.4$ the retardation after overload was more muted, with the growth rate dropping slightly immediately after overload before returning to the baseline rate after 1 mm of crack growth beyond overload. As at $R = 0.1$, there was no indication of an initial increase prior to the retardation.

(a) $R = 0.1$			(b) $R = 0.4$		
ΔK^{app}	N	$\Delta a/r_p^{OL}$	ΔK^{app}	N	$\Delta a/r_p^{OL}$
27.5	-1	0	27.6	-1	0
58.3	0	0	42.3	0	0
27.5	1	0	27.6	1	0
27.4	18k	0.3	28.1	3k	0.2
27.2	30k	0.6	27.7	5k	0.5
25.2	46k	1.0	27.9	10k	1.0
25.6	79k	1.6	28.2	18k	1.6

Table 2: ΔK^{app}, number of cycles beyond overload, N, and normalised crack growth beyond overload, $\Delta a/r_p^{OL}$ at which the strain maps were acquired. Δa is taken coincide with the midpoint of the leading-edge of the crack-tip stress gradient at max. load [18].

3.2. Fractography Analysis

Fractographs of the samples tested at $R = 0.1$ and $R = 0.4$ can be seen in Fig. 5 and Fig. 6 respectively. In each case the crack front immediately prior to overload is delineated by deformation and contact associated with the overload and is marked on the fractographs (this was most obvious at $R = 0.1$). The crack front prior to overload bowed slightly towards the free surfaces but in the central 3.5 mm (i.e. the EDXRD gauge length) it was essentially straight, with $< 100\,\mu\mathrm{m}$ variation in crack length being recorded. This lends further weight to the plane strain assumption.

At $R = 0.1$ a region of darker, compressed material clearly delineates the overload location. This deformation is associated with the contact of opposing crack faces and is consistent with features observed originally by Jones [36]. A large region of compressive contact and deformation is circled in Fig. 5c; this type of damage is seen to cover a large

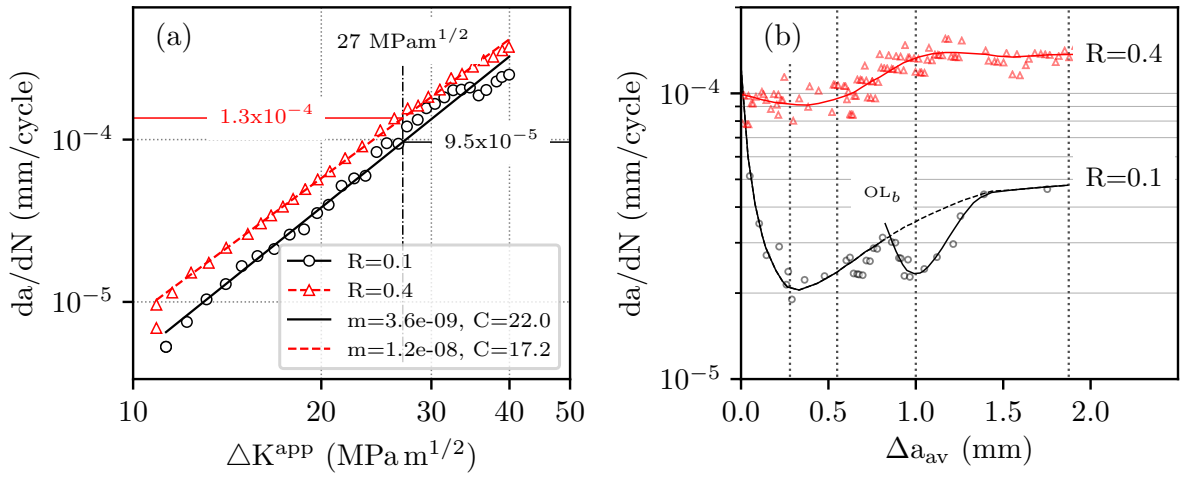

Figure 4: (a) Baseline fatigue crack growth curves (i.e. without overload) at $R = 0.1$ and $R = 0.4$. (b) AC-PD measured fatigue crack growth rate at $\Delta K^{app} = 27\,\mathrm{MPa\,m^{1/2}}$ as a function of crack growth beyond overload at $R = 0.1$ and $R = 0.4$. OL_b highlights the position of a second, accidental overload at $R = 0.1$. The vertical lines highlight the approximate EDXRD measurement locations.

proportion of the surface area in the material just ahead of overload. At mid-thickness the region of compressed material (the contact zone) extends approximately 300 µm beyond the overload location, with the contact zone at the sample surface being approximately 1.5 times this size. This is unsurprising given that the plastic zone in a plane stress state would be expected to be around 1.67 times larger than under plane strain conditions [28]. You would therefore expect a similar increase in the size of any deformed, contact zone. Note that although the position of the accidental overload, OL_b can be seen in Fig. 5b, there is no indication of contact occurring at this location and no deformation on the fracture surface.

After overload and at the end of the FCG testing the crack front has bowed significantly, with 1 mm of crack growth being recorded at the surface compared to 2.2 mm of growth mid-thickness. FCG retardation is therefore greater at the sample surface compared to the centre. This is consistent with the sample surface being in a state of plane stress, which promotes plasticity, overload residual stresses and PIC/discontinuous closure. This is, however, contrary to the observations made by Shuter et al. [5] and Borrego et al. [26], who noted slight crack bowing at the free surfaces both before and after overload but no increase in bowing upon overload. However, in both cases the crack was grown until the FCG rates had recovered i.e. beyond the point at which overload plasticity, residual stress and contact are effective. Once outside this region, the crack front would be expected to return to it's original shape (under constant ΔK conditions). In the current work (at $R = 0.1$) the FCG rates have not recovered prior to the end of testing and the crack front has not re-straightened.

While the impact of the overload cycle is apparent even at low magnifications at $R = 0.1$, this is not so at $R = 0.4$. At higher magnifications (see Fig. 6c) one can see some evidence of deformation at mid-thickness (a slight discontinuity on the fracture surface); this deformation does not, however, appear to be associated with crack face contact. Regions of compressive deformation, likely due to crack face contact, can be seen towards the sample surface. This can again be explained by the increase in plasticity found towards a free surface. The change in crack front profile observed at $R = 0.1$ is not mirrored at $R = 0.4$.

3.3. Evolution of the Stress Field

Fig. 7 shows the 2D crack opening stress fields, $\sigma_{yy}(x, y)$, calculated from the EDXRD strain data for the tests at (a) $R = 0.1$ and (b) $R = 0.4$. The maps are shown at K_{min} and K_{max} prior to, during and after overload. Although the maps provide a useful insight into the overload behaviour,

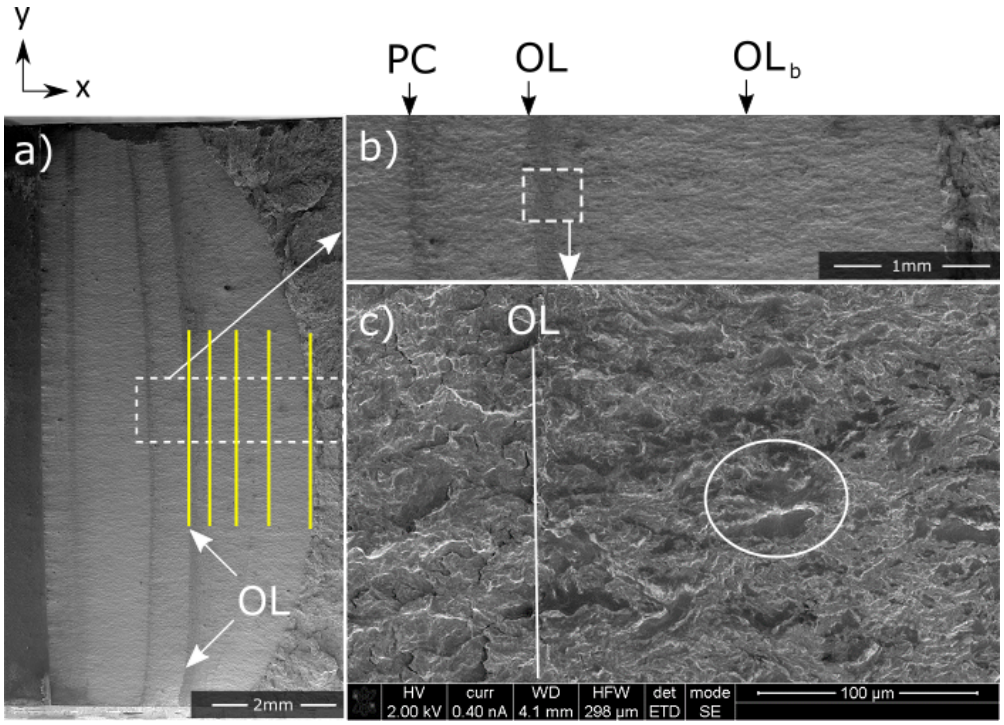

Figure 5: Fractographs from the experiment at $R = 0.1$. (a) Low magnification image of full crack face. (b) Higher magnification 1.5 mm slice through mid-thickness, with the notch, start of pre-crack (PC) and overload (OL) highlighted. (c) High magnification of the overload region; note the flattened, deformed regions to the right of the overload. White circle highlights a region of deformed material. The yellow, vertical bars highlight the crack-tip position at the different FCG/EDXRD acquisition stages, with the length of the bar defining the sampled gauge length.

line profiles through the maps are perhaps easier to compare. As such, line profiles taken at various positions and stages of unloading are presented in Fig. 8.

At $R = 0.1$ prior to overload, one can see a small reverse plastic zone at K^{app}_{min} (highlighted on Fig. 7a (i) and Fig. 8a). The reverse plastic zone increases in size and magnitude immediately after overload. This response is due to the additional plasticity and compressive residual stress introduced during loading to K^{OL} and is consistent with Eqn. 4 i.e. an increase in the cyclic plastic zone size due to a larger stress excursion ($\Delta K^{OL} > \Delta K$). This reduction in stress at K_{min} is mirrored at both K_{max} and at the intermediate loading levels. The overload residual stresses act across the full loading range, shifting the stress profiles down at all applied loads (as per Fig 1b and Fig 1c).

The crack-tip stress profiles at maximum load eventually recover as the crack is propagated beyond the overload position, with the stress profile acquired at K^{app}_{max} at the end of FCG ($\Delta a/r^{OL}_p = 1.6$) being roughly equivalent to that seen prior to overload (i.e. Fig. 7a (i) vs. Fig. 7a (iv)). The recovery occurs over a length scale that approximates to the theoretical overload plastic zone size; a more detailed assessment is presented in Section 4.1.

At $R = 0.4$ the impact of overload residual stresses on the acquired stress profiles (from K_{max} to K_{min}) is again evident immediately after overload. The crack-tip stress fields reduce in response to the overload residual stresses and again recover as the crack is propagated across a distance that is approximately equal to the theoretical overload plastic zone size. However, in this case, the shift in the stress profiles is less significant. This can be rationalised based on the overload factor, K^{OL}/K^{app}_{max}, which is much lower at $R = 0.4$ than at $R = 0.1$, and the associated relative change in crack-tip plasticity due to loading to K^{OL} compared to the nominal loading to K^{app}_{max}.

In addition to assessing the impact of the overload residual stresses it is important to look for crack face contact and the influence of both PIC and discontinuous closure. Immediately before and after overload there is no sign of contact behind

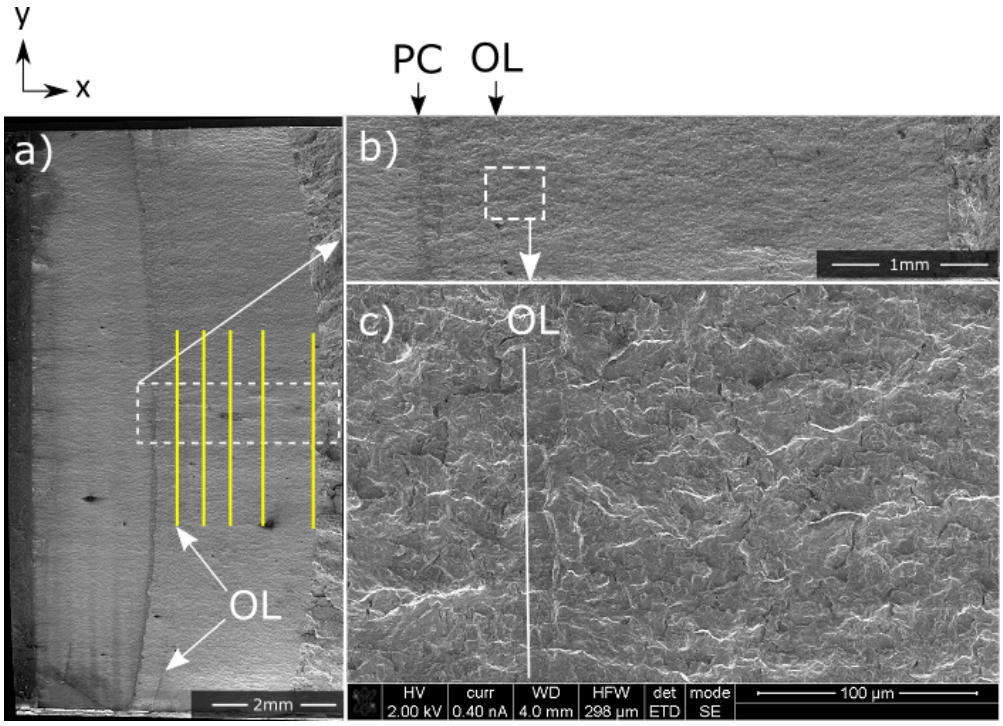

Figure 6: Fractographs from the experiment at $R = 0.4$. (a) Low magnification image of full crack face. (b) Higher magnification 1.5 mm slice through mid-thickness, with the notch, start of pre-crack (PC) and overload (OL) highlighted. (c) High magnification of the overload region; note the similarity between the fracture surface before and after OL. The yellow, vertical bars highlight the crack-tip position at the different FCG/EDXRD acquisition stages, with the length of the bar defining the sampled gauge length.

the crack-tip at either $R = 0.1$ or $R = 0.4$. This therefore suggests that PIC is not active under this set of conditions. This is consistent with observations made by Lopez-Crespo et al. [37] and may reflect the constraint associated with the plane strain stress state.

Although there is no evidence of PIC, discontinuous crack face contact is observed at $R = 0.1$ (not at $R = 0.4$). This behaviour can be seen at each of the EDXRD acquisition locations beyond the overload position, with the effects being clearest at the end of FCG, where $\Delta a/r_p^{OL} = 1.6$ (this is highlighted on Fig. 8d). The evidence for discontinuous closure is twofold; first we observe compressive contact stresses at the overload location, most notably at K_{min}^{app}. This stress is associated with contact and load transfer at the plastic asperity left in wake of the advancing crack front. The observed contact zone is similar to that highlighted on the EDXRD maps presented by Withers et al. [38] and is consistent with the compressive deformation seen on the fractographs presented in Section 3.2. Secondly, we see a reduction in the size and magnitude of the reverse plastic zone at K_{min}^{app} as compared to the stress profile taken at K_{min}^{app} prior to overload (compare Fig. 8a to Fig. 8d). This is indicative of the associated increase in K_{min}^{eff} and reduction in ΔK^{eff}. The development and changes in discontinuous contact stress are further explored in Section 4.2.

4. Discussion and Analysis

4.1. Variation in crack-tip stress

To better understand the impact of residual stress, PIC and discontinuous closure, it is helpful to consider the variation of the crack-tip stress during unloading as a function of crack position. The crack-tip is defined as the centre point of the leading-edge of the crack-tip stress gradient at maximum load (as per Croft [18]). With a finite gauge volume we cannot reliably measure the strain (and therefore stress) at the crack-tip but only in the vicinity. We therefore consider the stress averaged over a 200 µm window 250 µm ahead of the crack-tip. This position is close to the crack tip yet ensures that the sampled region is outside of the cyclic

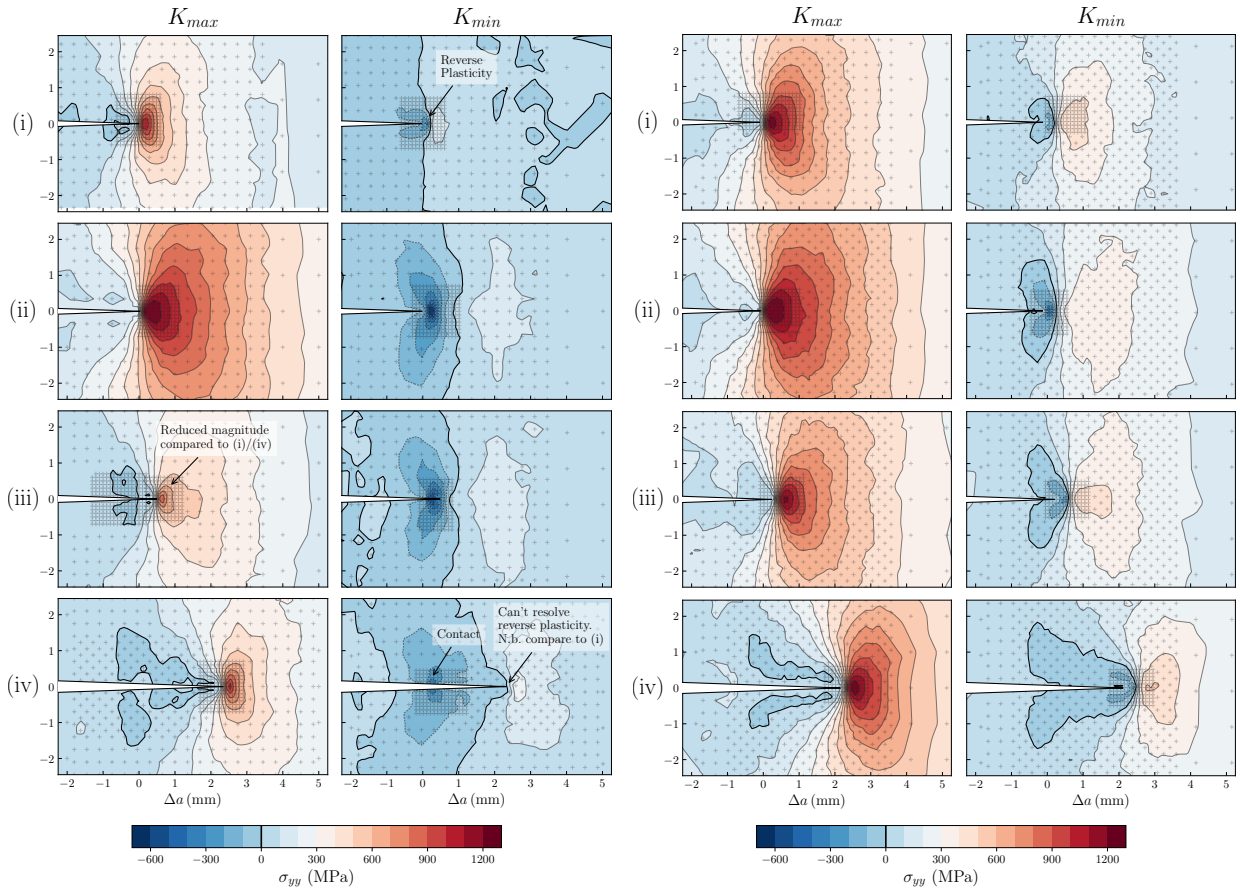

(a) $R = 0.1$ (b) $R = 0.4$

Figure 7: 2D stress maps measured at K_{max} (LHS) and K_{min} (RHS) at (a) $R = 0.1$ and (b) $R = 0.4$ for (i) one cycle before OL (ii) at OL (iii) when $\Delta a/r_p = 0.3$ and (iv) when $\Delta a/r_p^{OL} = 1.6$. The light grey crosses indicate acquisition points. The thicker, black contour lines delineate 0 MPa.

plastic zone ($r_c = 0.06\,\text{mm}$), which delimits the elastic-plastic boundary for cyclic plastic flow [39].

The variation in crack-tip stress is presented in Fig. 9. As expected, the relationship between crack-tip stress and applied load is linear at both $R = 0.1$ and $R = 0.4$ (although notably only where $K^{app} > 0.6K^{app}_{max}$ at $R = 0.1$). Furthermore, the rate of change of crack-tip stress with respect to increasing applied load is the same irrespective of crack growth past overload. This behaviour is to be expected from a simple LEFM standpoint.

After the overload cycle there is a mean stress effect at both $R = 0.1$ and $R = 0.4$ caused by the overload residual stress field, whereby the crack tip stresses are reduced relative to those before overload. Interestingly, immediately after overload, the crack-tip stress with respect to applied load is identical for the tests at $R = 0.1$ (Fig. 9a) and $R = 0.4$ (Fig. 9b) i.e. for the same applied load you induce the same crack-tip stress (note that this is not the case once the crack has been propagated beyond this position). For example, when $K^{app} = 20\,\text{MPa}\,\text{m}^{1/2}$, $\sigma_{yy} = 200\,\text{MPa}$ at both $R = 0.1$ and $R = 0.4$. This suggests that prior plasticity is essentially overwritten during the overload, which is consistent with the findings from finite element work carried out by Salvati et al. [8].

The initial reduction and subsequent recovery in crack-tip stress at $R = 0.1$ and $R = 0.4$ is summarised in Fig. 9c. This highlights the reduction in crack-tip stress state relative to the initial, nominal state i.e. $\sigma_{yy(OL+N)} - \sigma_{yy(OL-1)}$, where N is the number of cycles beyond overload. The change in σ_{yy} is taken from the mean shift in crack-tip stress

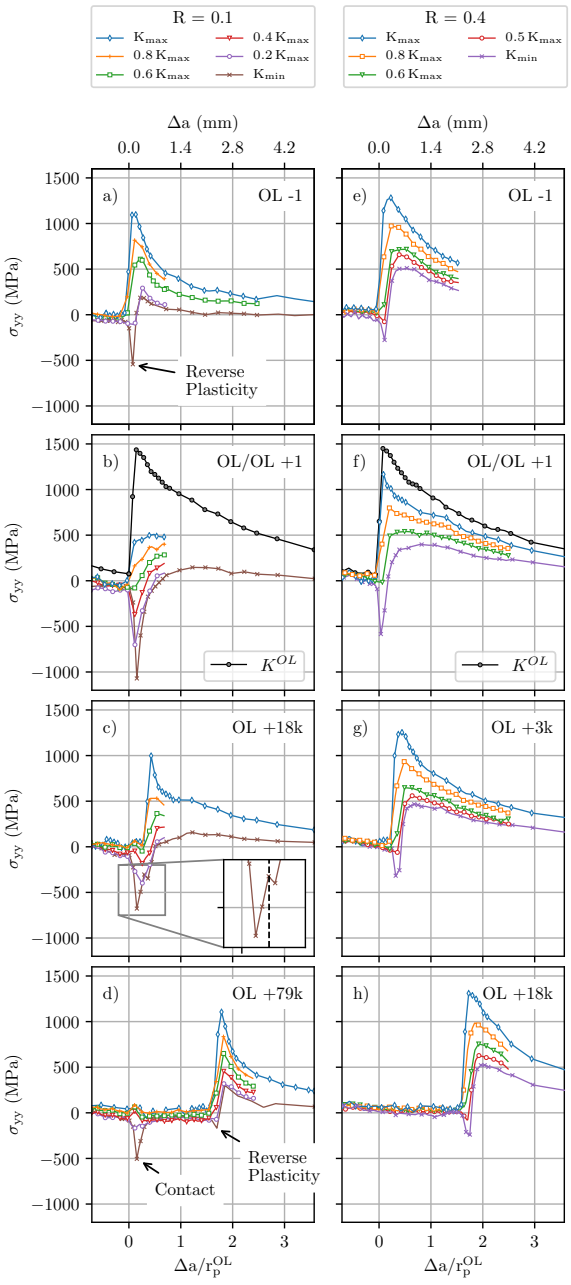

Figure 8: Stress profiles as a function of crack growth and applied load level for testing at (a-d) $R = 0.1$ and (e-h) $R = 0.4$. Profiles taken (a, e) one cycle before OL (b, f) at, and immediately after, OL (c, g) when $\Delta a/r_p = 0.3$ and (d, h) when $\Delta a/r_p^{OL} = 1.6$. Note that there are a reduced number of data points at some intermediate loads at $R = 0.1$ due to data acquisition issues.

where $K^{app} > 18\,\mathrm{MPa\,m^{1/2}}$ at $R = 0.1$ and across the full stress range at $R = 0.4$. Despite clear differences in the absolute reduction in crack-tip stress, both of the stress profiles recover over the same period, namely after 1.4 mm of FCG. The crack-tip stress recovery should occur in line with the plastic zone size (introduced at $K^{OL} = 60\,\mathrm{MPa\,m^{1/2}}$). Indeed, the measured value is similar to, albeit slightly larger than, the overload plastic zone size predicted by the calculations proposed by Irwin [28] ($r_p^{OL} = 1.17\,\mathrm{mm}$). Rather than using this theoretical value, we use the overload plastic zone size inferred from this experimental assessment of the recovery of crack-tip stresses to normalise the crack growth beyond overload (i.e. for $\Delta a/r_p^{OL}$, $r_p^{OL} = 1.4\,\mathrm{mm}$).

At the two applied load ratios we are essentially sampling the impact of overload factor, K^{OL}/K_{max}^{app}. So, while we are growing the crack through nominally the same overload residual stress field at both $R = 0.1$ and $R = 0.4$, which acts over the same length scale, r_p^{OL}, the actual significance of the overload residual stress field is governed by the crack tip plasticity associated with the nominal loading profile and, specifically, K_{max}^{app}. The importance of overload factor is expanded upon in Section 4.5.

The crack-tip stress response also provides further indirect confirmation of discontinuous closure at $R = 0.1$. Its influence can be seen at each acquisition location from $\Delta a/r_p^{OL} = 0.3$ (OL +18k) onwards. At these positions and when K^{app} is less than $18\,\mathrm{MPa\,m^{1/2}}$, the stress response is no longer linear with respect to applied load; the near crack-tip stresses are higher than would be anticipated and, as such, there is a reduction in the associated stress excursion. This should be considered indicative of a reduction in ΔK^{eff} due to an increase in K_{min}^{eff}. Lopez-Crespo et al. [19] have reported a similar reduction in the recorded strain range after an overload cycle. The inflection point at which the crack-tip stresses are no longer linear with respect to applied load should coincide with K^{op} and, physically speaking, first contact between the opposing crack faces. Interestingly, below K^{op} there is still a significant reduction in the crack-tip stress, which suggests that K^{op} cannot be considered to define the minimum effective stress intensity factor. This behaviour and the impact of discontinuous closure on K^{eff} is further considered in Section 4.2.

Note that K^{op} is approximately equal to K_{min}^{app} at $R = 0.4$. It is therefore unsurprising that there is no change in $\Delta\sigma_{yy}$ and no suggestion of crack closure after overload at $R = 0.4$.

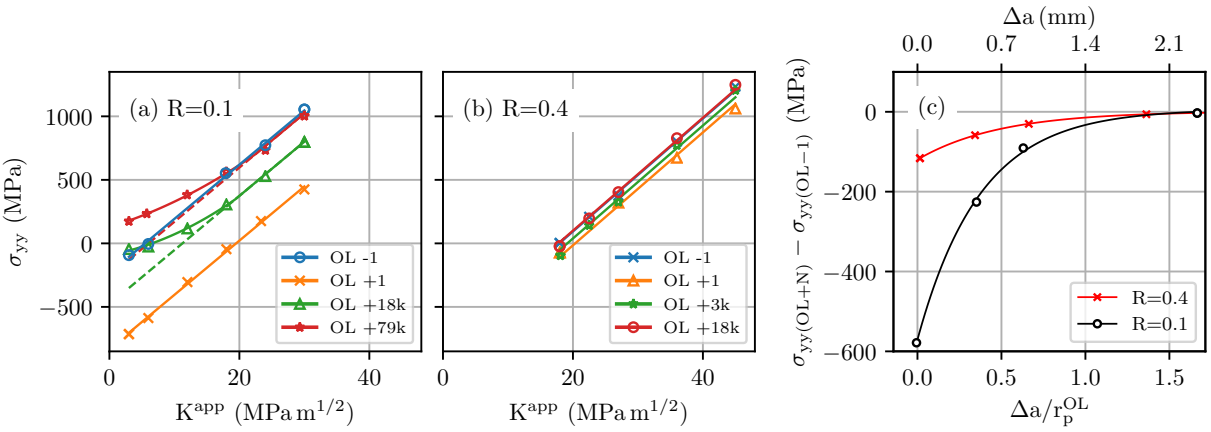

Figure 9: Near crack-tip stress state averaged across a 0.2 mm window at (a) $R = 0.1$ and (b) $R = 0.4$. Crack-tip stresses assessed as a function of K^{app} and number of cycles beyond overload. The reduction in crack-tip stress relative to initial level is shown in (c).

4.2. Estimation of the stress shielding from the crack face tractions

Crack face contact is traditionally characterised by the opening force and associated opening stress intensity factor, P^{op} and K^{op}. These values define the point at which the crack faces are completely separated (or first come into contact) and are regularly used to compute ΔK^{eff} [40]. Although there are numerous methods to define P^{op} [40], it is typically computed from changes in the compliance response. While a compliance type assessment (i.e. by tracking the change in stress gradient with respect to load) can be applied to the crack-tip stress data presented in Fig. 9, the EDXRD analysis presents us with the opportunity to take a more novel approach. In this case we can directly quantify the crack face traction forces and associated shielding by assessing the compressive, contact stresses recorded at the overload location, which is where discontinuous crack face contact occurs.

We have calculated the contact force, P^{tract} by integrating the compressive stresses recorded over the contact area (see Fig. 10a). This procedure was completed at each load increment from K^{app}_{min} to K^{app}_{max} for each of the six EDXRD acquisiton locations at both $R = 0.1$ and $R = 0.4$. This informs us how the contact force develops with applied load and crack growth beyond overload. It is worth noting that this methodology is only appropriate to assess for the impact of discontinuous closure, which is to say where the contact stresses are distinct and separate from the crack tip. Plasticity induced closure is characterised by contact occurring immediately behind the crack tip and in this scenario it would be very difficult to separate reverse plasticity and contact stresses. There is, however, no evidence of PIC either before overload or when $\Delta a/r_p > 0.3$, i.e. where EDXRD measurements were made.

Fig. 10b highlights the change in P^{tract} as a function of applied load after the crack has been grown to a position $\Delta a/r_p^{OL} = 0.3$ beyond overload. K^{op} has also been marked on Fig. 10b at the point the crack face traction force rises above 0 kN. This approach suggests that $K^{op} = 18\,\mathrm{MPa\,m^{1/2}}$, which corroborates the results presented in Section 4.1. At $R = 0.4$, $K^{app}_{min} \geq K^{op}$; discontinuous closure is therefore not expected to be an active shielding mechanism at this load ratio. Note that while 0 kN should be the maximum recorded value for the crack face tractions, the sampled area is finite (not a continuum point) and will weakly reflect changes in K^{app}.

P^{tract} is the (average) force acting to keep the crack open across the EDXRD gauge length. If we assume that P^{tract} acts as a point load at a distance, Δa from the crack tip, in a sample of width, $W' = W - a_0$, we can estimate the associated stress intensity factor, K^{tract} from compliance calculations used to assess a CT geometry:

$$K^{tract} = -f\left(\frac{\Delta a}{W'}\right)\frac{P^{tract}}{B\sqrt{2\pi W'}}. \qquad (9)$$

$f(\Delta a/W')$ is calculated according to the closed form expression presented by Xiao et al. [41], which

is valid for shallow cracks. The geometry we have used is detailed in Fig. 3b.

K^{tract} is a direct measure of the shielding associated with crack face contact for a given applied stress intensity factor. This is particularly important given that we see load transfer to/from the crack tip when $K^{app} < K^{op}$ (Section 4.1). We must therefore specifically characterise the shielding at K^{app}_{min}, which is an approach previously adopted by Weiss, Chen and Stickler [42], who defined this as the shielded stress intensity factor range ΔK^{sh}. In our case this is equivalent to the stress intensity factor associated with the crack face tractions at minimum load, K^{tract}_{min}. The associated minimum shielded stress intensity factor, $K^{sh} = K^{tract}_{min} + K^{app}_{min}$, is analogous, but not equal, to K^{op}.

The crack shielding due to discontinuous crack face contact as a function of crack growth beyond overload is shown in Fig. 10c. It is interesting to note that the shielding at minimum load is significantly smaller than the opening stress intensity factor. For example, after the final FCG increment at $R = 0.1$, $K^{sh} = 7.5\,\mathrm{MPa\,m^{1/2}}$ whereas the opening stress intensity factor was approximately $18\,\mathrm{MPa\,m^{1/2}}$. While surprising, this finding is consistent with the trends highlighted in the crack-tip stress analysis presented in Fig. 9a, with approximately 30 % of the total crack-tip stress excursion occurring below K^{op}. This reaffirms what was previously suggested, K^{op} should only be considered to define first contact at high points along the length of the plastically deformed asperity; it does not well predict the amount of shielding from discontinuous closure.

4.3. Stress intensity factor arising from residual stress

If we assume the driving force contribution to be negligible when $K^{eff} < 0\,\mathrm{MPa\,m^{1/2}}$ (as per Willenbourg [4]), we can begin to quantify the retardation from the overload residual stress field if we calculate the stress intensity factor arising from it, K^{res}. K^{res} can be calculated from a known residual stress distribution and a geometry specific weight function, $h(a, x)$. Fett and Munz [43] defined an expression for the CT geometry, which is given in Eqn. 10, and is both convenient to calculate and valid for both short and long crack lengths:

$$h(a,x) = \frac{1}{\Omega}\left[1 + \sum_{v}^{\mu} \frac{A_{v,\mu}\left(\frac{a}{W}\right)^2}{\left(1-\frac{a}{W}\right)^{\frac{3}{2}}}\left(1-\frac{x}{a}\right)^n\right] \quad (10)$$

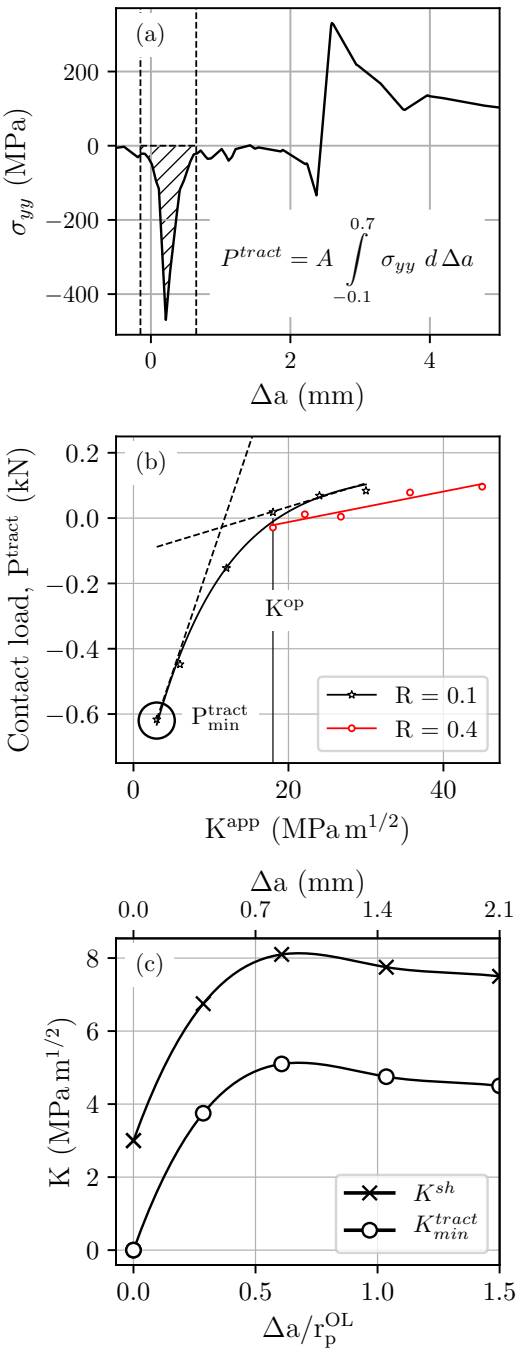

Figure 10: (a) Methodology for calculating P^{tract} from contact stresses observed at the overload location. (b) Contact load, P^{tract} for $R = 0.1$ and $R = 0.4$ as a function of K^{app}, evaluated when $\Delta a/r_p^{OL} = 0.3$. (c) K^{tract}_{min} as a function of crack growth at $R = 0.1$, calculated from the contact force at minimum load.

where

$$\Omega = \sqrt{2\pi a}\sqrt{1-\frac{x}{a}}.$$

The parameters v, μ and A_v, can be taken from the work by Fett and Munz [43]. a/W is the ratio of crack length to sample width and x is the position along the crack length. In turn, K^{res} can be calculated according to Eqn. 11:

$$K_I = \int_0^a \sigma_{yy}(x)\; h(a,x)\, dx \qquad (11)$$

One can only apply Eqn. 11 to a balanced stress field i.e. the net stress is zero, with significant error being introduced if this does not hold true [44]. As such, to calculate K^{res} from the stress profiles acquired during this experiment, the stress field associated with K^{app} must be accounted for. In this case a simple Williams type approach [45] was used to estimate the applied stress field, which was subtracted from the measured field. The associated, underlying σ^{res} distribution was then verified by asserting that $\sum \sigma^{res}_{yy} = 0\,\text{MPa}$. The residual stress field seen in Fig. 11a was calculated from the stresses acquired immediately after overload at K^{app}_{min} at $R = 0.1$. Given that the residual stress profile is defined by the plasticity introduced at K^{OL}, it will be equally applicable to the experiments at both $R = 0.1$ and $R = 0.4$. The prior crack-tip plasticity is overwritten by the plasticity introduced at K^{OL}.

K^{res} was calculated from the stress profile shown in Fig. 11a according to Eqn. 11 and is presented in Fig. 11b. K^{res} reaches a minimum value of $-14.5\,\text{MPa}\,\text{m}^{1/2}$ shortly after overload, before tending back to zero just beyond the end of the overload plastic zone. It is important to note that the peak value (although not the general trend) of K^{res} is sensitive to the precise choice of crack-tip location. A shift of $\pm 50\,\mu\text{m}$ alters the maximum calculated value of K^{res} by $\pm 3\,\text{MPa}\,\text{m}^{1/2}$.

Fig. 11b not only depicts K^{res} but also highlights other factors that will likely determine the FCG behaviour. For $R = 0.4$, we can see that the stress intensity factor arising from the overload residual stresses is smaller in magnitude than the applied stress intensity factor and therefore is not large enough to cause residual stress induced crack shielding (i.e. Fig. 1b vs. Fig. 1c). Furthermore, $K^{app}_{min} \geq K^{op}$, which tells us that there is no shielding from discontinuous crack face contact. We can therefore reasonably assume that ΔK^{eff} is unaffected by the overload cycle and any changes in

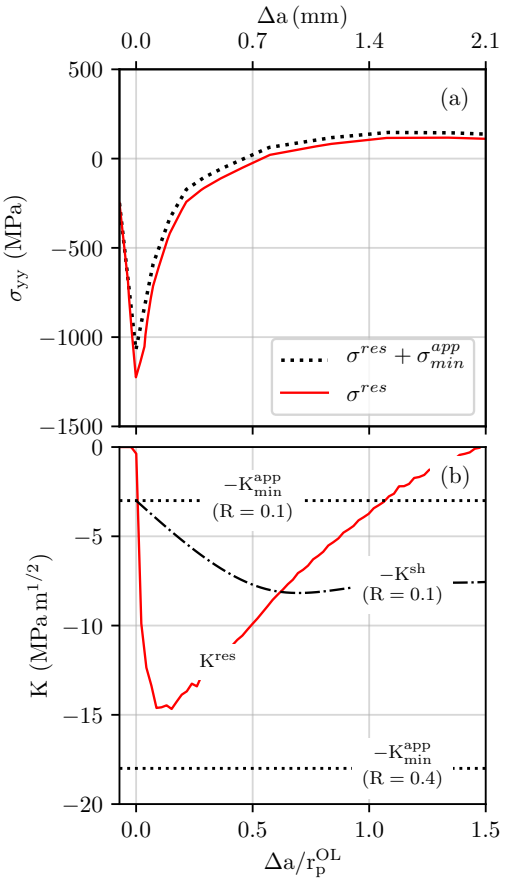

Figure 11: (a) σ^{res} as a function of crack growth beyond overload and (b) the associated value of K^{res}. Note that the values of K^{app}_{min} at $R = 0.1$ and $R = 0.4$, along with K^{op} at $R = 0.1$ are also displayed.

FCG behaviour are linked solely to changes in R^{eff}. This is explored further in Section 4.4.

The comparable assessment at $R = 0.1$ predicts a competition between shielding from overload residual stresses and discontinuous closure. While these mechanisms occur concurrently, we suggest that ΔK^{eff} is determined by a single shielding mechanism, rather than by the combination of the two mechanisms, as suggested by Salvati et al. [8]. If, for example, the stress intensity factor associated with the crack face tractions is greater in magnitude than the stress intensity factor arising from the overload residual stress field, then K^{eff}_{min} will remain above 0. In this instance we wouldn't be in a regime where residual stress induced shielding, as defined by Willenborg [4], is active (Fig.1b). We can therefore say that shielding from crack face

tractions will dominate when

$$K^{res} + K^{sh} > 0 \tag{12}$$

and residual stresses will control crack shielding when

$$K^{res} + K^{sh} < 0. \tag{13}$$

The dominant shielding mechanism varies with position relative to the overload location. At shorter crack lengths, overload residual stresses dominate, while at longer crack lengths (and outside the overload plastic zone), discontinuous closure is the dominant shielding mechanism. The transition between these two regimes occurs when $\Delta a / r_p^{OL} = 0.6$, which can be seen in Fig. 11b. These general trends and the idea of a mechanistic transition are consistent with results presented by Lopez-Crespo et al. [19]and Salvati et al. [8].

4.4. Predicting retardation from ΔK^{eff}, R^{eff}

Having calculated the residual stress intensity distribution, along with the shielding/tractions associated with discontinuous crack face contact, we are able to estimate ΔK^{eff} with respect to crack growth beyond overload at both $R = 0.1$ and $R = 0.4$ (see Fig. 12a). The associated value of R^{eff} is displayed in Fig. 12b. Note that in this instance K^{eff} and R^{eff} are being truncated at 0 under the assumption that no FCG contribution is expected from the portion of the loading cycle where $K^{eff} < 0\,\mathrm{MPa\,m^{1/2}}$ [4, 15].

As discussed in Section 4.3, there is no apparent reduction in ΔK^{eff} after overload for the experiment at $R = 0.4$. R^{eff} does, however, drop to approximately 0.1 before ultimately tending back to the applied value just beyond the edge of the overload plastic zone. For $R = 0.1$, there are changes in both ΔK^{eff} and R^{eff}. The effective stress intensity range drops to $15.5\,\mathrm{MPa\,m^{1/2}}$ soon after overload and, significantly, does not fully recover over the measured crack growth beyond overload, plateauing at approximately $22.5\,\mathrm{MPa\,m^{1/2}}$. This is due to the continued influence of discontinuous closure (far beyond the edge of the plastic zone) and is consistent with previous research [8, 19].

The information presented in Fig. 12a and Fig. 12b can be used to predict da/dN, in accordance with a two-parameter Walker type FCG assessment. In this case we use the method proposed by Dinda and Kujawski [15], which only considers the positive portion of the fatigue cycle, which they

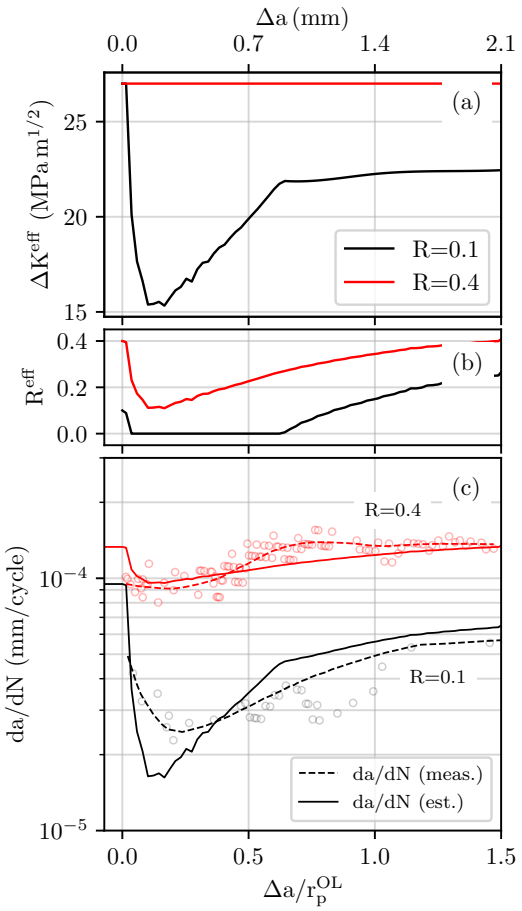

Figure 12: (a) ΔK^{eff} as a function of position relative to overload, estimated from values of K^{app}, K^{res} and K^{tract}_{min} for tests at $R = 0.1$ and $R = 0.4$ with the associated values of R^{eff} shown in (b). The resultant estimated values of da/dN calculated as per Dinda and Kujawski [15] are shown in (c), and are compared against the measured values of da/dN.

term as ΔK^{+}, but is equivalent in this assessment to ΔK^{eff}, such that

$$\frac{da}{dN} = \left[\left(\Delta K^{eff} \right)^{(1-p)} \left(K^{eff}_{max} \right)^{p} \right]^{\gamma}. \tag{14}$$

The resultant, predicted values of da/dN are presented in Fig. 12c. These predicted results are compared against the measured growth rates. For $R = 0.4$ the maximum level of retardation is well predicted by the estimated values of ΔK^{eff} and R^{eff}, with the main discrepancy between measured and predicted growth being the period over which the FCG rates recover. The predicted recovery occurs over the full FCG experiment, whereas the measured values are seen to recover to the base-

line level when $\Delta a/r_p^{OL} = 0.65$. One of the main assumptions of the weight function approach is that the crack-tip plasticity is small relative to the residual stresses. At $R = 0.4$ the forward plastic zone is around half the size of the overload plastic zone, this could lead to a redistribution of the residual stresses as the crack is propagated.

At $R = 0.1$ the agreement between the measured and estimated values of da/dN is very good in the regime where closure dominates i.e. towards the edge of, and then beyond, the overload plastic zone. When the crack growth beyond overload is small ($\Delta a/r_p < 0.6$) there is a larger discrepancy between measured and estimated values of da/dN. While this difference may be attributed to errors in K^{res} arising from redistribution of residual stress or inaccuracies in the diffraction elastic constants, it is important to stress that the difference in crack growth rates only represents a 15 % error in terms of ΔK^{eff} (or approximately 2.5 MPa m$^{1/2}$). Such discrepancy has been accepted to be satisfactory in previous works aimed at estimating ΔK^{eff} [46, 47, 48]. Furthermore, the overall trend in estimated and measured values of da/dN are consistent and support the suggestion of a transition from crack shielding dominated by overload residual stresses to discontinuous closure.

The agreement between the measured values of da/dN and the predicted values of da/dN goes a long way towards validating both the overall methodology and the measured values of K_{min}^{tract} and K^{res}. Significantly, this is the first time that FCG rates have been estimated on the basis of direct measurements of the shielding mechanisms and associated changes in the effective R-ratio. In short, we have been able to build up an accurate picture of the prevailing conditions at the crack tip at mid-thickness and shown that ΔK^{eff} is defined by the dominant shielding mechanism at a given position while R^{eff} varies as a function of the combined effect of both mechanisms.

4.5. Predicting retardation mechanisms as a function of overload factor and R

By separating and quantifying the retardation mechanisms we are also able to begin to piece together a generalised picture of the role of different overload retardation mechanisms as a function of overload factor (K^{OL}/K_{max}^{app}) and load ratio, R. Fig. 13 shows a schematic of the zones of influence of the various overload retardation mechanisms (as detailed in Fig. 1). Three regimes are defined in terms of applied load ratio and overload factor. For a large load ratio and low overload factor, which we define as regime (i), the retardation after overload is controlled by the overload residual stresses. In regime (i) the overload residual stresses lower the effective load ratio, R^{eff}, but are not severe enough to reduce the effective stress intensity factor range, ΔK^{eff} (as per Fig. 1b). This behaviour is consistent with the overload response described at $R = 0.4$ (overload factor of 1.33) and leads to minimal FCG retardation. In this regime the impact of the overload cycle, and subsequent retardation, will be limited to the size of the overload plastic zone.

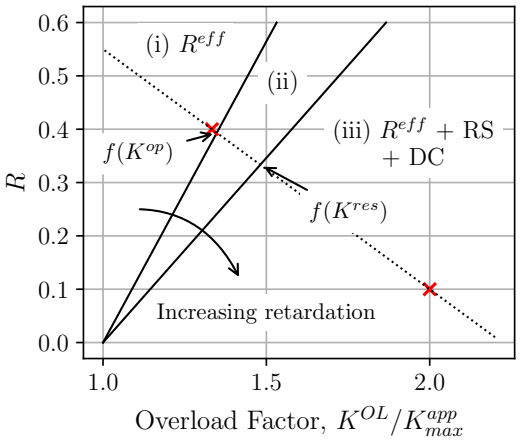

Figure 13: Overload retardation mechanism regimes as a function of overload factor and R (under constant ΔK conditions). Post-overload FCG retardation is ascribed to a combination of, and competition between, changes in R^{eff} and shielding from overload residual stresses (RS) and discontinuous closure (DC), the balance of which varies with regime. A single shielding mechanism is expected to operate in regime (ii). The red crosses highlight the tests carried out at $R = 0.1$ and $R = 0.4$ and the dotted line that connects them highlights the potential variability in overload factor and R under constant ΔK, constant K^{OL} conditions.

In regime (iii), which is also highlighted in Fig. 13, the effects of overload residual stress and discontinuous closure can broadly be considered to be in competition. So, while both mechanisms will affect R^{eff} only one, controlling mechanism, will determine changes in ΔK^{eff}. The controlling mechanism will vary with respect to crack growth beyond overload, with overload residual stresses dominating when the crack is shorter and within the overload plastic zone while discontinuous closure will control changes in ΔK^{eff} towards the edge of the overload plastic zone and outside of this region. Regime (iii) is found under high overload

factor and low load ratio conditions and would be expected to induce significant FCG retardation (as was seen during testing at $R = 0.1$).

Fig. 13 also details an intermediate region, regime (ii), that serves as a transition between regimes (i) and (iii). In this regime we assume that either overload residual stresses or discontinuous closure will be the sole active shielding mechanism. The upper and lower boundaries for this regime will coincide with the points at which K_{min}^{app} is equal K^{op} and/or the maximum absolute value of K^{res}. We can estimate where the boundary between regimes should fall if we assume that overload residual stresses and the associated deformation at the overload site are fixed under a constant value of K^{OL}. If we then simply vary R then the points at which (a) $K_{min}^{app} = K^{op}$ and (b) $K_{min}^{app} + K^{res} = 0$ can be used to predict the boundaries between regimes (see Fig. 13). The results presented in this work suggest that regime (ii) will only be active across a relatively narrow range of conditions as the maximum absolute values of K^{res} and K^{op} are closely matched (approximately $15\,\mathrm{MPa\,m^{1/2}}$ and $18\,\mathrm{MPa\,m^{1/2}}$ respectively). They also suggest that discontinuous closure will be the sole active mechanism in this intermediate regime ($K^{op} > -K^{res}$); uncertainty in these values and lack of test data does, however, make it difficult to reach a definitive conclusion on this point.

While the retardation regime boundaries and the schematic as a whole should be considered an initial approximation, this approach does represent a first step towards a parametric understanding and breakdown of overload and the associated, underlying retardation mechanisms.

5. Conclusions

We have considered the impact of overload and R-ratio on residual stress, closure mechanisms and thereby FCG retardation in a bainitic steel. Our aim has been to quantify the relative impact and contribution of different retardation mechanisms, notably residual stress driven shielding [4], plasticity induced closure [1] and discontinuous closure [2] through high energy, synchrotron EDXRD. The experiment used a constant stress intensity factor range and fixed overload stress intensity factor in contrast with previous research which used a constant overload factor, thereby varying K^{OL}, and/or utilised a constant load range [8, 23]. Both approaches have their merits, but by keeping ΔK^{app} and K^{OL} constant (similar to Borrego et al. [26]) we were able to fix the extrinsic conditions while controlling overload plastic zone size and the associated residual stress distribution. This allowed us to systematically assess the impact of R-ratio and overload factor, with the cracks being grown through the same deformation zone under nominally the same driving force. Most notably, we were, for the first time, able to directly measure the crack tip shielding arising from crack face tractions. In turn we have been able to predict FCG retardation based on direct measures of shielding.

- At both $R = 0.1$ and $R = 0.4$ there was a reduction in the peak crack-tip stress immediately after overload (most significantly at $R = 0.1$). This was due to the residual stress field introduced during the overload, with recovery of the crack-tip stresses occurring over a length scale (1.4 mm) consistent with the overload plastic zone size.

- The effect of overload residual stresses on K^{eff} was assessed using a weight function approach. This highlighted residual stress induced shielding at $R = 0.1$ but not at $R = 0.4$. This was the dominant shielding mechanism at $R = 0.1$ when crack growth beyond overload was small and while the crack remained within the overload plastic zone ($\Delta a / r_p^{OL} < 0.6$).

- Although there was no indication of plasticity induced closure, discontinuous crack face contact was recorded at $R = 0.1$. This was due to a plastic asperity associated with the overload cycle. Discontinuous closure was the dominant shielding mechanism when the crack had been propagated towards the edge of, and also beyond, the overload plastic zone. Discontinuous closure was not active at $R = 0.4$ as the opening stress intensity factor was less than the minimum applied stress intensity factor.

- For the first time, the shielding associated with the discontinuous crack face tractions, K^{tract}, have been computed directly from the measured contact stresses (at $R = 0.1$). The shielding calculated from the crack face tractions is much lower than would be suggested from the opening stress intensity factor; significant load transfer to and from the crack tip was observed while $K^{app} < K^{op}$.

- In addition to retardation arising from a reduction in ΔK^{eff}, changes were observed in FCG behaviour due to a variation in R^{eff}. This variation is due to the concurrent influence of crack face tractions and overload residual stresses, the effects of which are particularly apparent at $R = 0.4$, where there is no change in ΔK^{eff}.

- The predicted internal (plane strain) FCG rates calculated according to a two-parameter Walker type assessment based on K^{app}, K^{res} and K^{tract}_{min}, well explained the measured FCG values. Further, complementary work is now ongoing to describe material in a plane stress state, i.e. at the sample surface.

Acknowledgements

We thank Diamond Light Source for access to beamline I12:JEEP (E12205) that contributed to the results presented here. This work was also made possible by the facilities and support provided by the Research Complex at Harwell, funded in part by the EPSRC (EP/I02249X/1). Thanks also go to JFE for both the material and their technical expertise. PJW is grateful to the European Research Council for funding COREL-CT under grant No. 695638. Financial support of Spanish Ministerio de Educacin, Cultura y Deporte through mobility grant José Castillejo and Spanish Ministerio de Economia y Competitividad through grant reference MAT2016-76951-C2-2-P is also acknowledged.

References

[1] W. Elber, Fatigue crack closure under cyclic tension, Engineering Fracture Mechanics 2 (1) (1970) 37–45. doi:10.1016/0013-7944(70)90028-7.

[2] N. A. Fleck, Influence of stress state on crack growth retardation, Basic Questions in Fatigue: Volume I (1988) 577–593.

[3] P. J. Withers, P. Lopez-Crespo, A. Kyrieleis, Y. Hung, Evolution of crack-bridging and crack-tip driving force during the growth of a fatigue crack in a Ti/SiC composite, Proceedings of the Royal Society A: Mathematical, Physical and Engineering Sciences 468 (2145) (2012) 2722–2743. doi:10.1098/rspa.2012.0070.

[4] J. Willenborg, R. M. Engle, H. A. Wood, A crack growth retardation model using an effective stress concept, Technical memorandum 71-1-FBR (1971) 1–22.

[5] D. M. Shuter, W. Geary, Some aspects of fatigue crack growth retardation behaviour following tensile overload in structural steel, Fatigue & Fracture of Engineering Materials and Structures 19 (2-3) (1996) 185–199. doi:10.1111/j.1460-2695.1996.tb00958.x.

[6] R. O. Ritchie, Mechanisms of fatigue crack propagation in metals, ceramics and composites: Role of crack tip shielding, Materials Science and Engineering 103 (1) (1988) 15–28. doi:10.1016/0025-5416(88)90547-2.

[7] T. Anderson, Fracture mechanics: fundamentals and applications, 3rd Edition, CRC Press, Florida, 2005.

[8] E. Salvati, H. Zhang, K. S. Fong, X. Song, A. M. Korsunsky, Separating plasticity-induced closure and residual stress contributions to fatigue crack retardation following an overload, Journal of the Mechanics and Physics of Solids 98 (2017) 222–235. doi:10.1016/j.jmps.2016.10.001.

[9] S. Suresh, Fatigue of Materials, Cambridge University Press, Cambridge, 1998. doi:10.1017/CBO9780511806575.

[10] B. Budiansky, J. W. Hutchinson, Analysis of Closure in Fatigue Crack Growth, Journal of Applied Mechanics 45 (2) (1978) 267. doi:10.1115/1.3424286.

[11] J. Newman, A Crack-Closure Model for Predicting Fatigue Crack Growth under Aircraft Spectrum Loading, in: J. Chang, C. Hudson (Eds.), Methods and Models for Predicting Fatigue Crack Growth Under Random Loading, ASTM International, West Conshohocken, PA, 1981, pp. 53–84. doi:10.1520/STP28334S.

[12] R. Pippan, A. Hohenwarter, Fatigue crack closure: a review of the physical phenomena, Fatigue and Fracture of Engineering Materials and Structures 40 (4) (2017) 471–495. doi:10.1111/ffe.12578.

[13] M. Beghini, L. Bertini, Fatigue crack propagation through residual stress fields with closure phenomena, Engineering Fracture Mechanics 36 (3) (1990) 379–387. doi:10.1016/0013-7944(90)90285-0.

[14] K. Walker, The Effect of Stress Ratio During Crack Propagation and Fatigue for 2024-T3 and 7075-T6 Aluminum, in: M. Rosenfeld (Ed.), Effects of Environment and Complex Load History on Fatigue Life, ASTM International, West Conshohocken, PA, 1970, pp. 1–14. doi:10.1520/STP32032S.

[15] S. Dinda, D. Kujawski, Correlation and prediction of fatigue crack growth for different R-ratios using Kmax and K+ parameters, Engineering Fracture Mechanics 71 (12) (2004) 1779–1790. doi:10.1016/j.engfracmech.2003.06.001.

[16] A. H. Noroozi, G. Glinka, S. Lambert, A two parameter driving force for fatigue crack growth analysis, International Journal of Fatigue 27 (10-12) (2005) 1277–1296. doi:10.1016/j.ijfatigue.2005.07.002.

[17] C. S. Shin, N. A. Fleck, Overload retardation in a structural steel, Fatigue & Fracture of Engineering Materials and Structures 9 (5) (1987) 379–393. doi:10.1111/j.1460-2695.1987.tb00464.x.

[18] M. Croft, Z. Zhong, N. Jisrawi, I. Zakharchenko, R. Holtz, J. Skaritka, T. Fast, K. Sadananda, M. Lakshmipathy, T. Tsakalakos, Strain profiling of fatigue crack overload effects using energy dispersive X-ray diffraction, International Journal of Fatigue 27 (10-12) (2005) 1408–1419. doi:10.1016/j.ijfatigue.2005.06.022.

[19] P. Lopez-Crespo, A. Steuwer, T. Buslaps, Y. H. Tai, A. Lopez-Moreno, J. R. Yates, P. J. Withers, Measuring overload effects during fatigue crack growth in bainitic steel by synchrotron X-ray diffraction, International Journal of Fatigue 71 (2015) 11–16. doi:doi.org/10.1016/j.ijfatigue.2014.03.015.

[20] A. J. Allen, M. T. Hutchings, C. G. Windsor, C. Andreani, Neutron diffraction methods for the study of

residual stress fields, Advances in Physics 34 (4) (1985) 445–473. doi:10.1080/00018738500101791.

[21] J. E. Allison, The measurement of crack tip stresses by X-ray diffraction (AFFDL-TR-78-24), Tech. rep., Air Force Flight Dynamics Laboratory, Wright-Patterson Air Force Base, Ohio, USA (1978).

[22] A. Steuwer, M. Rahman, A. Shterenlikht, The evolution of crack-tip stresses during a fatigue overload event, Acta Materialia 58 (11) (2010) 4039–4052. doi:10.1016/j.actamat.2010.03.013.

[23] J. P. Belnoue, T. S. Jun, F. Hofmann, B. Abbey, A. M. Korsunsky, Evaluation of the overload effect on fatigue crack growth with the help of synchrotron XRD strain mapping, Engineering Fracture Mechanics 77 (16) (2010) 3216–3226. doi:10.1016/j.engfracmech.2010.08.018.

[24] ASTM International, ASTM E8/E8M-16a, Standard Test Methods for Tension Testing of Metallic Materials, Tech. rep., ASTM International, West Conshohocken, PA (2016). doi:10.1520/E0008.

[25] ASTM International, ASTM E647-15e1, Standard Test Method for Measurement of Fatigue Crack Growth Rates, Tech. rep., ASTM International, West Conshohocken, PA (2015). doi:10.1520/E0647-15E01.2.

[26] L. Borrego, J. Ferreira, J. Pinho da Cruz, J. Costa, Evaluation of overload effects on fatigue crack growth and closure, Engineering Fracture Mechanics 70 (11) (2003) 1379–1397. doi:10.1016/S0013-7944(02)00119-4.

[27] M. R. Rowles, On the calculation of the gauge volume size for energy-dispersive X-ray diffraction, Journal of synchrotron radiation 18 (6) (2011) 938–41. doi:10.1107/S0909049511033267.

[28] G. R. Irwin, Plastic Zone Near a Crack and Fracture Toughness, in: Proceedings of the 7th Sagamore Ordnance Materials Research Conference, Racquette Lake, NY, 1960, pp. 63–78.

[29] M. Drakopoulos, T. Connolley, C. Reinhard, R. Atwood, O. Magdysyuk, N. Vo, M. Hart, L. Connor, B. Humphreys, G. Howell, S. Davies, T. Hill, G. Wilkin, U. Pedersen, A. Foster, N. De Maio, M. Basham, F. Yuan, K. Wanelik, I12: the Joint Engineering, Environment and Processing (JEEP) beamline at Diamond Light Source, Journal of Synchrotron Radiation 22 (3) (2015) 828–838. doi:10.1107/S1600577515003513.

[30] C. A. Simpson, A. Cinar, P. Lopez-Crespo, S. Kozuki, M. Mostafavi, P. J. Withers, The effect of stress state and R-ratio on fatigue overload behaviour [to be submitted].

[31] P. J. Withers, M. Preuss, A. Steuwer, J. W. L. Pang, Methods for obtaining the strain-free lattice parameter when using diffraction to determine residual stress, Journal of Applied Crystallography 40 (5) (2007) 891–904. doi:10.1107/S0021889807030269.

[32] A. M. Korsunsky, K. E. Wells, P. J. Withers, Mapping two-dimensional state of strain using synchroton X-ray diffraction, Scripta Materialia 39 (12) (1998) 1705–1712. doi:10.1016/S1359-6462(98)00385-6.

[33] C. A. Simpson, pyxe: XRD Strain Analysis (apr 2016). doi:10.5281/zenodo.50185.

[34] M. Mostafavi, D. M. Collins, M. J. Peel, C. Reinhard, S. M. Barhli, R. Mills, M. B. Marshall, R. S. Dwyer-Joyce, T. Connolley, Dynamic contact strain measurement by time-resolved stroboscopic energy dispersive synchrotron X-ray diffraction, Strain 53 (2) (2017) 1–13. doi:10.1111/str.12221.

[35] M. T. Hutchings, P. J. Withers, T. M. Holden, T. Lorentzen, Introduction to characterization of residual stress by neutron diffraction, 1st Edition, CRC Press, 2005.

[36] R. Jones, Fatigue crack growth retardation after single-cycle peak overload in Ti-6Al-4V titanium alloy, Engineering Fracture Mechanics 5 (3) (1973) 585–604. doi:10.1016/0013-7944(73)90042-8.

[37] P. Lopez-Crespo, P. J. Withers, F. Yusof, H. Dai, A. Steuwer, J. F. Kelleher, T. Buslaps, Overload effects on fatigue crack-tip fields under plane stress conditions: surface and bulk analysis, Fatigue & Fracture of Engineering Materials & Structures 36 (1) (2013) 75–84. doi:10.1111/j.1460-2695.2012.01670.x.

[38] P. J. Withers, Fracture mechanics by three-dimensional crack-tip synchrotron X-ray microscopy, Philosophical Transactions of the Royal Society A: Mathematical, Physical and Engineering Sciences 373 (2036) (2015) 1–26. doi:10.1098/rsta.2013.0157.

[39] J. R. Rice, Mechanics of Crack Tip Deformation and Extension by Fatigue, in: Fatigue Crack Propagation, Vol. ASTM STP 4, ASTM International, West Conshohocken, PA, 1967, pp. 247–311. doi:10.1520/STP47234S.

[40] S. Stoychev, D. Kujawski, Methods for crack opening load and crack tip shielding determination: A review, Fatigue and Fracture of Engineering Materials and Structures 26 (11) (2003) 1053–1067. doi:10.1046/j.1460-2695.2003.00691.x.

[41] Q. Xiao, B. Karihaloo, Coefficients of the crack tip asymptotic field for a standard compact tension specimen, International Journal of Fracture 118 (1) (2002) 1–15. doi:doi.org/10.1023/A:1022618930492.

[42] D. L. Chen, B. Weiss, R. Stickler, A model for crack closure, Engineering Fracture Mechanics 53 (4) (1996) 493–509. doi:10.1016/0013-7944(95)00169-7.

[43] T. Fett, D. Munz, Stress intensity factors and weight functions, Computational Mechanics Publications, 1997.

[44] R. Bao, X. Zhang, N. A. Yahaya, Evaluating stress intensity factors due to weld residual stresses by the weight function and finite element methods, Engineering Fracture Mechanics 77 (13) (2010) 2550–2566. doi:10.1016/j.engfracmech.2010.06.002.

[45] M. L. Williams, On The Stress Distribution at the Base of a Stationary Crack, Journal of Applied Mechanics 24 (1) (1956) 109–114.

[46] A. D. Nurse, E. A. Patterson, Determination of Predominantly Mode II Stress Intensity Factors from Isochromatic Data, Fatigue & Fracture of Engineering Materials and Structures 16 (12) (1993) 1339–1354. doi:10.1111/j.1460-2695.1993.tb00743.x.

[47] F. A. Díaz, J. R. Yates, E. A. Patterson, Some improvements in the analysis of fatigue cracks using thermoelasticity, International Journal of Fatigue 26 (4) (2004) 365–376. doi:10.1016/j.ijfatigue.2003.08.018.

[48] P. Lopez-Crespo, A. Shterenlikht, E. A. Patterson, J. R. Yates, P. J. Withers, The stress intensity of mixed mode cracks determined by digital image correlation, Journal of Strain Analysis for Engineering Design 43 (8) (2008) 769–780. doi:10.1243/03093247JSA419.